Wideband Dual-Polarized Endfire Slotted Horn Antenna With Tightly Coupled Dipole and Monopole Probe Arrays

Seongjung Kim, *Member, IEEE*, Young-Seok Lee, *Graduate Student Member, IEEE*, and Sangwook Nam, *Life Senior Member, IEEE*

***Abstract*—In this work, we present a novel wideband dual-polarized endfire array antenna for 5G millimeter-wave (mmWave) applications. The antenna design combines a tightly coupled dipole array (TCDA) for horizontal polarization and a tightly coupled monopole probe array (TCMPA) with a slotted metal horn for vertical polarization to achieve wideband operation. The slotted metal horn enhances the radiation and impedance matching of the TCMPA and makes operation of both polarizations in the same aperture. Both the TCMPA and TCDA operate at 23.8–42.3 GHz (< −10 dB for broadside radiation, fractional bandwidth = 56%) which covers n258 (24.25–27.5 GHz), n257 (26.5–29.5 GHz), n261 (27.5–28.35 GHz), and n260 (37–40 GHz) in frequency range 2 (FR 2) specified by 3GPP. This wideband operation can be made possible by incorporating the proposed polarization-selective reflectors which optimize the performance of both the TCMPA and TCDA. Under same phase excitation, simulated array gains of the vertical and horizontal polarizations manifest as 4–8 and 4.4–8.2 dBi, respectively. When scanning up to 45° from the array axis, those are degraded to 4.6–7.2 and 4.6–5.6 dBi, respectively. Experimental results, including matching bandwidth, realized array gain, and radiation pattern, were compared with simulated results and they were in good agreement. Finally, we highlighted the comparative advantages of our proposed array that operates in FR 2, compared with dual-polarized endfire linear array antennas operating over wideband.**

***Index Terms*—5G, dual-polarization, endfire, horn antenna, millimeter-wave (mmWave), tightly coupled dipole array (TCDA), tightly coupled monopole probe array (TCMPA), wideband.**

I. Introduction

THE rapid development of wireless communication technologies has led to the emergence of fifth-generation (5G) cellular networks, which aim to meet growing demands for higher data rates, lower latency, and greater network capacity. A key enabler of these objectives is the adoption of millimeter-wave (mmWave) frequency bands, which offer abundant spectrum resources for high-speed data transmission [1], [2], [3], [4], [5]. In particular, the frequency range 2 (FR 2), spanning from 24.25 to 52.6 GHz, has been designated for 5G mmWave mobile handsets [6]. To overcome the inherent high path loss of mmWave signals, beamforming techniques are widely used to enhance gain and coverage [7]. Among various antenna configurations, end-fired linear arrays have gained significant attention for their ability to steer wide fan-beams across the 3-D spatial domain, especially when mobile terminals are backed by metal covers or held in the hand, where front-facing planar arrays struggle to provide sufficient coverage [8].

However, the end-fired linear arrays have challenges due to a thin configuration of the printed circuit board (PCB) [9], [10], [11], [12], [13], [14], [15], [16], [17]. In fact, thin configuration limits the impedance bandwidth, particularly for vertical polarization [9], [10], [11], because of the large discontinuity of the characteristic impedance between the thin PCB with a small impedance and the free space with a high impedance [12]. This abrupt impedance discontinuity limits the matching bandwidth. To address this, several designs introduced metallic loading structures to artificially increase the effective thickness of the aperture, thereby achieving wider impedance bandwidths. For dual-polarized end-fired arrays, cavity-backed apertures, slotted substrate-integrated waveguides (SIWs), or L-shaped probes are used to support both vertical and horizontal polarizations limited in a thin configuration. While these designs successfully implement dual-polarization, their operational bandwidth remains narrow, generally under 27%, due to their thin configuration [13], [14], [15], [16]. On the other hand, [17] achieved a wider bandwidth of 26.9% using bulky metal-loaded structures that simultaneously induce parallel electric and magnetic resonances, thereby alleviating the high impedance of free space and smoothing the abrupt impedance transition between the antenna and free space [18]. However, this bandwidth is still insufficient to cover a wide range of the FR 2 band.

The tightly coupled array concept is implemented by introducing a large capacitance between the dipole or monopole arms and placing them close to a grounded reflector to achieve wideband operation [19], [20], [21]. In this work, we propose a novel dual-polarized wideband end-fired antenna array that integrates a tightly coupled dipole array (TCDA)

Received 18 December 2024; revised 6 July 2025; accepted 20 July 2025. Date of publication 30 July 2025; date of current version 30 October 2025. This work was supported by the Institute of Information and Communications Technology Planning and Evaluation (IITP) through Korean Government (MSIT) (Advanced And Integrated Software Development For Electromagnetic Analysis) under Grant 2019-0-00098. *(Corresponding author: Sangwook Nam.)*

The authors are with the Institute of New Media Communication (INMC), School of Electrical and Computer Engineering, Seoul National University, Seoul 08826, South Korea (e-mail: sjkim@ael.snu.ac.kr; ryanlee@snu.ac.kr; snam@snu.ac.kr).

Digital Object Identifier 10.1109/TAP.2025.3592276

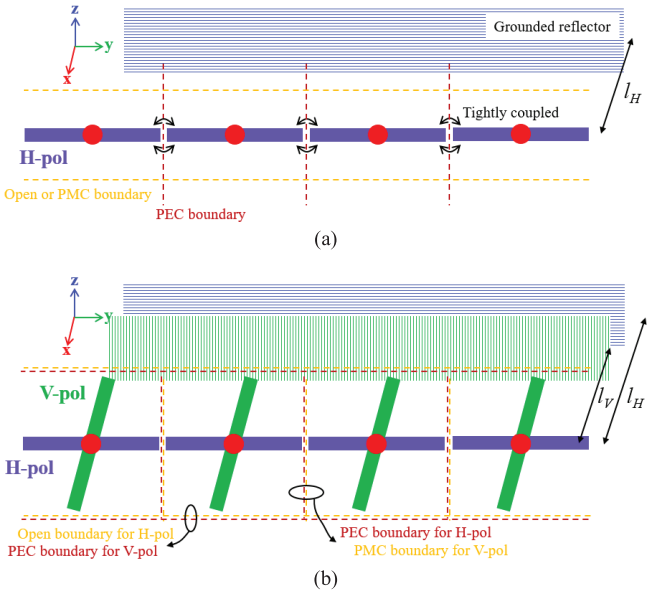

Fig. 1. Tightly coupled array concept. (a) Horizontally polarized linear array antenna and virtual boundary condition. (b) Dual-polarized linear array antenna and virtual boundary condition.

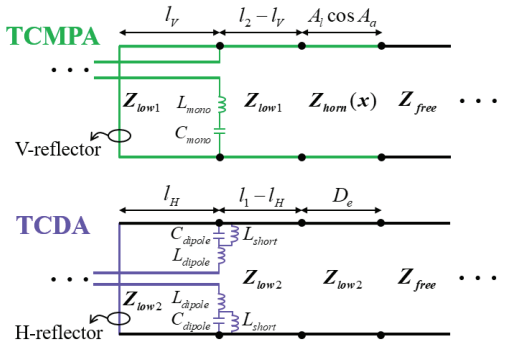

Fig. 2. Equivalent circuits of the proposed dual-polarized unit cell structure.

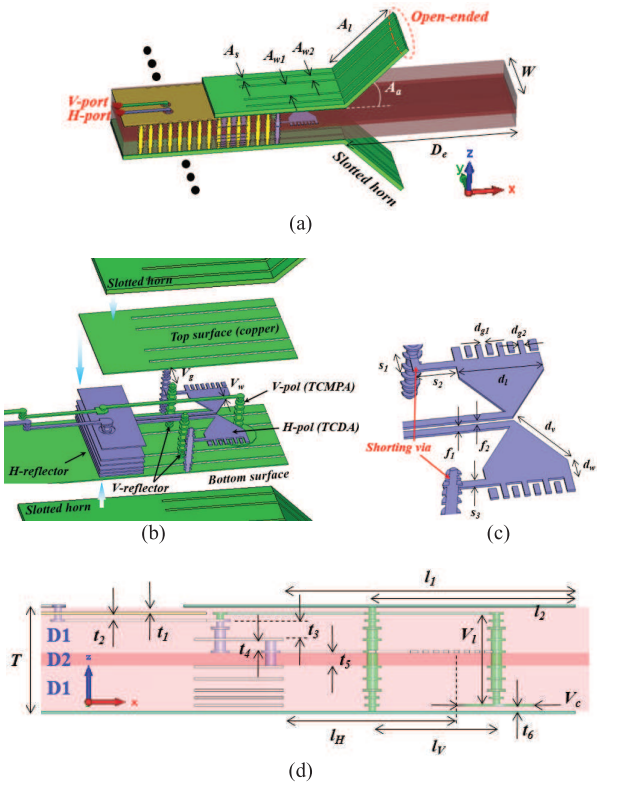

Fig. 3. Proposed unit cell for infinitely periodic structure in the y-direction. Green and blue structures are essential to enable TCMPA and TCDA to operate, respectively. (a) Perspective view of the full structure. (b) Exploded inner view. (c) Enlarged TCDA view. (d) Side view without side vias.

[19], [20] for horizontal polarization and a tightly coupled monopole probe array (TCMPA) [21] for vertical polarization within a shared aperture. This dual-polarized antenna cannot be simply achieved by integrating them. Tightly coupled element basically requires perfect electric conductor (PEC) boundary condition between them, whereas open or perfect magnetic conductor (PMC) boundary condition is necessary on the sides in the z-direction [see Fig. 1(a)]. Therefore, the integration is inherently challenging since their polarizations require different boundary conditions on the same side [see Fig. 1(b)] without cross-polarization interference. Furthermore, it requires different optimized distances to the grounded reflector [l_H and l_V in Fig. 3(d)]. To address this, we introduce a slotted horn structure to simultaneously satisfy the double boundary condition (open for H-pol and PEC for V-pol) and efficient radiation of the V-pol. In addition, a polarization-selective reflector (V-reflector for V-pol, an H-reflector for H-pol) is proposed to achieve individual optimization of the operating bandwidths. As detailed in Section II, this is essential for enabling tightly coupled operation in both the polarizations. This polarization-selective structure differentiates our work from previous efforts such as [15], where dipole and monopole elements are also used, but not in a tightly coupled or independently optimized manner. Consequently, our design achieves a significantly wider operating bandwidth—from 23.8 to 42.3 GHz—enabling robust dual-polarized operation across n258 (24.25–27.5 GHz), n257 (26.5–29.5 GHz), n261 (27.5–28.35 GHz), and n260 (37–40 GHz) of the FR 2 spectrum.

The remainder of this article is organized as follows. Section II describes the design of the proposed unit cell structures, including the TCMPA, TCDA, and slotted horn. The polarization-selective mechanism is also analyzed in detail through parametric studies. Section III presents simulated and measured results of the fabricated 1×4 array, highlighting impedance matching and gain characteristics. Finally, Section IV concludes this article with a summary of key findings.

II. Design of Antenna Structure and Operation

Basically, tightly coupled dipole or monopole probe array operates across the wideband with help of strong interaction of the series L and C, and the grounded reflector [19], [20], [21]. Fig. 2 shows the equivalent circuits of the proposed structure for V- and H-pol cases. For instance, at low-frequency band, the grounded reflector located at the distance of l_V or l_H from the TCMPA and TCDA provides inductive energy (shorter than quarter wavelength), while the series L and C provides capacitive energy (lower than resonance frequency). On the

TABLE I
DIMENSIONS OF THE PROPOSED UNIT CELL STRUCTURE (UNIT: MM)

A_a	A_l	A_s	A_{w1}	A_{w2}	D_e	W	T
45°	2	0.05	0.51	0.25	4	1.6	0.86
V_g	V_w	V_1	V_c	l_V	l_H	l_1	l_2
0.4	0.06	0.71	0.6	0.98	1.33	2.5	1.6
t_1	t_2	t_3	t_4	t_5	t_6	f_1	f_2
0.04	0.04	0.13	0.08	0.1	0.04	0.38	1.86
s_1	s_2	s_3	d_l	d_w	d_v	d_{g1}	d_{g2}
0.2	0.33	0.06	0.65	0.18	0.57	0.04	0.04

other hand, at high-frequency band, the grounded reflector provides capacitive energy (longer than quarter wavelength), while the series L and C provides inductive energy (higher than resonance frequency). In fact, a series resonator with large capacitance and small inductance can achieve wideband operation, as it exhibits slow variation with frequency due to its impedance characteristics (slope: jL and $1/jC$). To realize this, small element spacing is used to achieve low inductance, and large parallel-plate or interdigital structures are used to obtain high capacitance. It should be noted that the optimized length of l_V or l_H should be different since the different geometry of the TCMPA and TCDA produces different L and C. The proposed unit cell structure consists of a TCMPA, a TCDA, and the slotted horn as shown in Fig. 3(a). Moreover, the extended dielectric with a length of D_e improves the radiation of horizontally polarized wave. The horn is made of stainless-steel 304 with open-ended slots of width A_s. Thereby, the slotted walls look like open boundary to the H-pol (TCDA) and PEC boundary to the V-pol (TCMPA), achieving the boundary condition (z-direction) as explained in Fig. 1(b). In addition, the PEC and PMC boundary conditions between the elements are satisfied by linearly arraying the unit elements in the y-direction. Red circles at the left end indicate discrete ports with 50-Ω impedance for excitation to the TCMPA and the TCDA. Fig. 3(b) illustrates exploded view of the unit cell without the dielectric layers. While the TCMPA has one arm to be excited, the TCDA has two arms which are excited unevenly. Therefore, the dipole arms should be connected to grounded vias with shorting vias (L_{short}) to avoid common mode generation [22]. The stacked PCB layers consist of 12 metal layers with dielectrics (D1): 970LF(LD) (ε_r = 3.2 $tan\delta$ = 0.004) and a core material (D2): 972LF(LD) (ε_r = 3.4 $tan\delta$ = 0.004). All the structural dimensions of the proposed unit cell structure are listed in Table I.

For wideband operation, the TCMPA consists of a vertical via at the right side and a large circular pad for producing a self-inductance (L_{mono}) and a large capacitance (C_{mono}), respectively [21]. As an important point, it operates with optimized distance from the grounded V-reflector [see Fig. 7(a)] and radiates by smooth impedance transition ($Z_{horn}(x)$ in Fig. 2) from the thin PCB (Z_{low1}) to the air (Z_{free}), thanks to the horn structure [11]. Fig. 4 shows surface current distribution on the inner structure at two different instances when the two discrete ports are excited independently. When the TCMPA is excited, the current flows only through the single microstrip line to the monopole probe, which does not

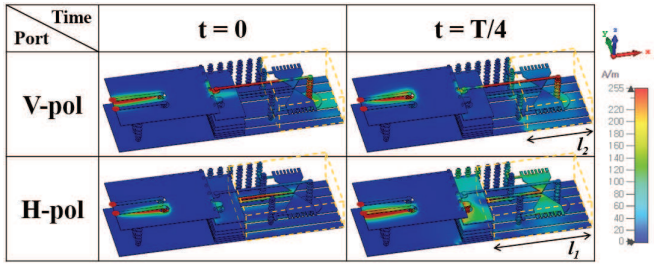

Fig. 4. Surface current distribution on the inner structure at 32 GHz is shown at two different instances when the TCMPA and TCDA are excited. T represents a time period. Note the large current flows on the vertical monopole probe and the horizontal dipole for the V-port (TCMPA) and the H-port (TCDA) excitation, respectively.

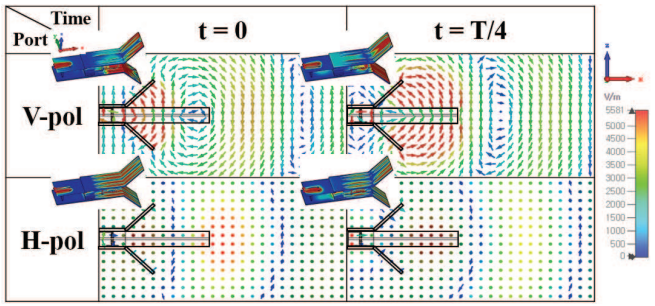

Fig. 5. Electric field distribution viewed from the side without the side vias at 32 GHz is shown at two different times when the V-port (TCMPA) and the H-port (TCDA) are excited.

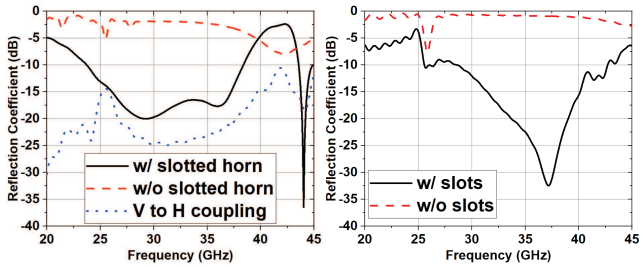

Fig. 6. Reflection coefficients of the unit cell (a) when the V-port (TCMPA) is excited with and without the horn and (b) H-port (TCDA) is excited with and without the slots.

couple to the dipole at any times. Furthermore, the induced current on the bottom surface is consistently strong (it is on the top surface as well). That implies that the top and bottom surfaces are imperative for operation of the TCMPA. At t = T/4, due to reflection of the backward wave radiating from the monopole, it is observed that another current is induced on the V-reflector. Two vias in V-reflector are sufficient to block the backward wave. For the TCDA in Fig. 3, for wideband operation, the TCDA necessitates a large capacitance and such like that of the TCMPA, which is attained through interdigital capacitance (C_{dipole}) compensated by self-inductance (L_{dipole}), as depicted in Fig. 3(c). It requires the optimized distance from the grounded H-reflector [see Fig. 7(b)] as well. The proposed H-reflector and V-reflector configuration can simultaneously satisfy the both the optimized distances since the V-reflector is polarization-selective; in other words, it reflects

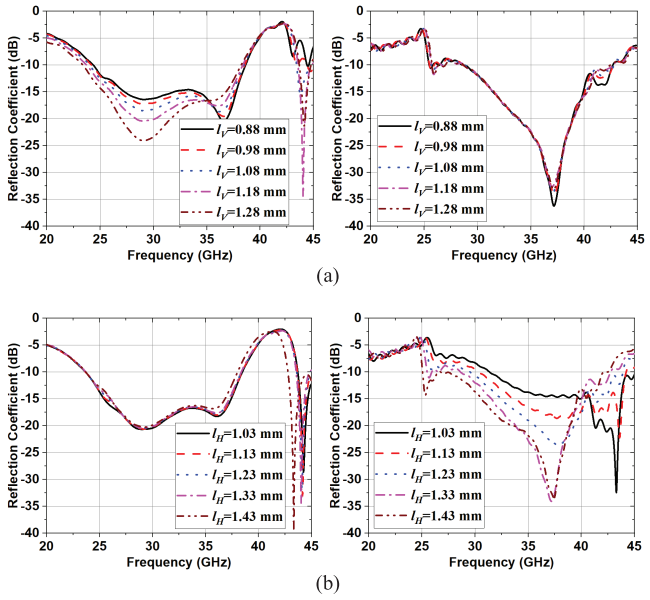

Fig. 7. Parametric study on GND position, (a) l_V and (b) l_H, when the positions of the TCMPA and TCDA are fixed. Left and right columns are corresponding to the V-port (TCMPA) and the H-port (TCDA) excitations, respectively.

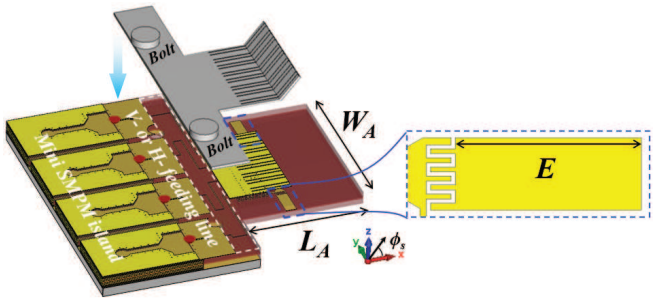

Fig. 8. Exploded view of the proposed 1 × 4 finite array configuration considering the arrangement of mini SMPMs and the horn (W_A = 10.3, L_A = 8.1, and E = 1.8 mm).

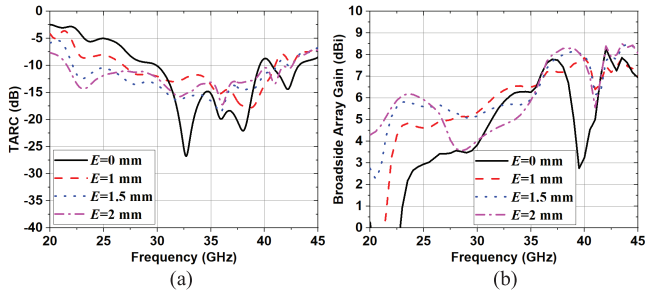

Fig. 9. Parametric study on the extended side arm, E, of the finite array. (a) TARCs of the TCDA and (b) broadside array gains.

the vertical polarization only. The extended dielectric slab of length D_e helps impedance matching of the dipole (it can be confirmed soon). In Fig. 4, for H-pol excitation, likewise, the current flows only through the single microstrip line and the coplanar strip lines to the dipole arms, without coupling to the monopole at any time. In this case, there is no induced current on the V-reflector, but on the H-reflector. This is because backward wave radiating from the dipole is not scattered at the V-reflector while it is scattered at the H-reflector. Two plates in H-reflector are sufficient to block the backward wave.

In Fig. 5, electric field distribution viewed from the side is depicted without the side vias. When the TCMPA is excited, vertically polarized electric field radiates out of the slotted horn aperture and the extended dielectric. There are four noteworthy observations in Fig. 5. First, the electric field distribution appears relatively weak at the outer slots of the horn. Second, within the structure, the electric field is confined in the right side of the V-reflector. Third, the electric field experiences significant diffraction by the horn. Finally, the electric field distribution exhibits discontinuities at the dielectric boundary, resulting from the boundary condition where any vertical electric displacement should be continuous at the boundary. When the TCDA is excited, on the horn, strong electric field appears only at the slots owing to its transmission. In addition, the electric field is confined in the right side of the H-reflector, within the structure. Furthermore, it radiates out in a focused manner along the extended dielectric. Effects of the slots and the slotted horn for both the polarizations are investigated as shown in Fig. 6. In Fig. 6(a), the reflection coefficient at the TCMPA is poor if the slotted horn is not used. However, the thin aperture of the TCMPA can be smoothly transitioned and effectively matched to wide free space by the slotted horn. Consequently, impedance matching is successively achieved as depicted in that figure. In addition, mutual coupling between the two ports is presented to be less than −15 dB below 40 GHz. In Fig. 6(b), the reflection coefficient at the TCDA is seriously degraded without the slots due to the boundary condition (z-direction) as explained before. However, the slots transmit the horizontal polarization as the open boundary.

III. Simulated and Experimental Results for the Proposed Full Array Antenna

The proposed 1 × 4 array antenna with a center-to-center element spacing of W [in Fig. 3(a)] is presented in Fig. 8. To excite the array, mini subminiature push-on micros (SMPMs) operating up to 40 GHz are used, and two prototypes for excitation to the TCMPA and TCDA are separately designed which are identical structure except only for the feeding lines. Moreover, the horn is configured to be mounted on the PCB and fixed by the bolts. According to the well-known finite array design, the property of a finite array is somewhat different with that of an infinite array, particularly for strong mutually coupled antennas such as the TCDA since it can operate by assistance of the mutual coupling which is absent for the edge elements of a finite array [24], [25]. Therefore, additional structures are required to make the finite array be similar to the infinite array [24], [25]. In the figure, the structure are the interdigitally coupled additional dipole arms with a length of E. This additional arm provides two effects for the TCDA: the improvement of the impedance matching of the finite array and an increase in the array gain as described in Fig. 9, where the total active reflection coefficient (TARC) is a terminology similar to a reflection coefficient [26]. In addition,

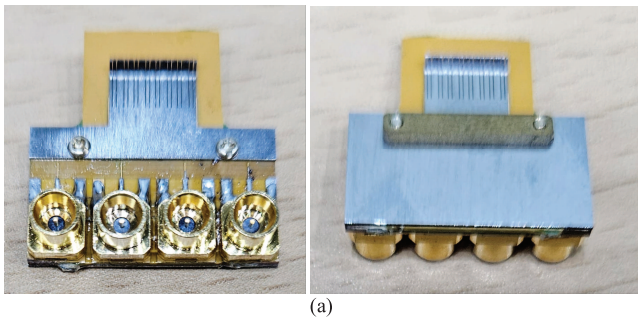

(a)

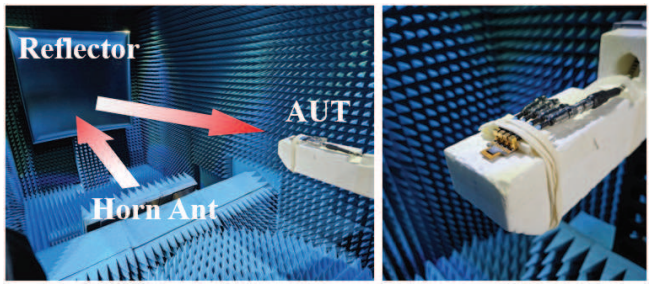

(b)

Fig. 10. (a) Fabricated prototype of the proposed 1 × 4 array. (b) Measurement setup for a beam pattern of the array in far-field condition.

there is an optimal value of E for impedance matching and gain.

In Fig. 10(a), fabricated prototype of the proposed array is shown, and measurement of the radiation pattern is performed in the anechoic chamber with the reflector for making far-field distance as described in Fig. 10(b). In fact, the mini SMPMs and the connected feeding lines to the array can introduce ohmic losses and some reflections, as the recommended PCB material and thickness specified in the data sheet are not exploited. Therefore, to examine the array antenna, they should be calibrated by the method (using direct and extended-thru lines) [26]. The radiation patterns are postprocessed by superposition of complex active element gain patterns [27], and the gain losses by the connectors and lines are calibrated by the same way [26].

Fig. 11 shows the simulated and measured scattering parameters, TARCs, and radiation efficiency. The simulation result is obtained by full-wave simulation of the 1 × 4 array, and the mini SMPM model is not included since the measured result is in the same condition excluding the connectors calibrated by the method [26]. In Fig. 11(a), self-scattering parameters are not sufficiently low level since the proposed antenna can operate with the help of mutual coupling from adjacent elements. In this case, the mutual coupling is around −10 dB (cannot be negligible level), resulting in low active reflection coefficient (e.g., $S_{11} + S_{12} + S_{13} + S_{14}$). The TARC includes the mutual coupling effect by simultaneous excitation. Under the condition of TARC ≤ −10 dB, simulated impedance matching bandwidths for vertical and horizontal polarizations with $\phi_s = 0°$ are 23.8–42.3 and 21.8–42.7 GHz, respectively. And overlapped bandwidth of them is 23.8–42.3 GHz (56%). When scanning to $\phi_s = 45°$, those are well-preserved, remaining below −6 dB within that frequency range. And the radiation efficiency is well-preserved

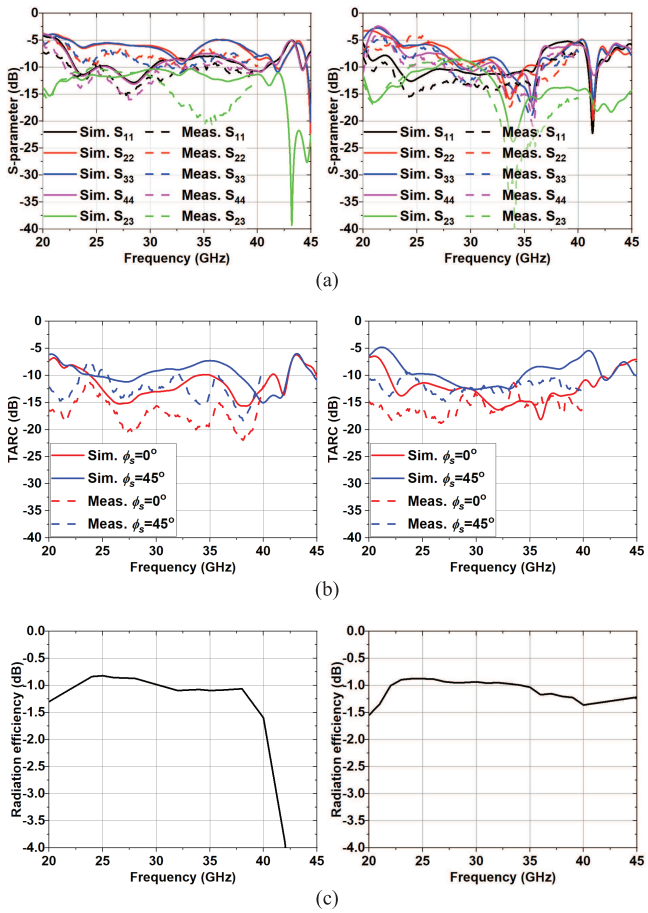

Fig. 11. Simulated and measured (a) scattering parameters and (b) TARC as scanning the beam from $\phi_s = 0°$ to $\phi_s = 45°$, and (c) simulated radiation efficiency. Left and right columns are corresponding to the V-port (TCMPA) and the H-port (TCDA) excitations, respectively.

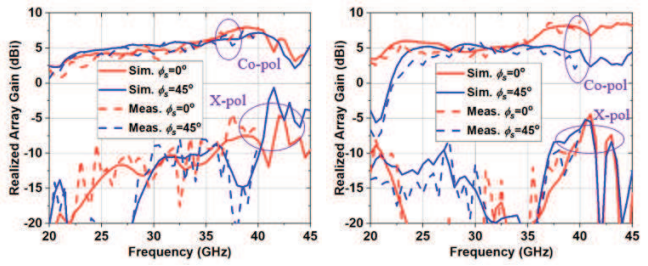

Fig. 12. Simulated and measured realized array gains as scanning the beam from $\phi_s = 0°$ to $\phi_s = 45°$. Left and right columns are corresponding to the V-port (TCMPA) and H-port (TCDA) excitations, respectively.

around −1 to −1.5 dB. Fig. 12 presents the array gains when steering the beam from $\phi_s = 0°$–$45°$. At the overlapped frequency band, the simulated array gains of the V-pol and H-pol manifest as 4–8 and 4.4–8.2 dBi, respectively. And the measured realized gain is following the behavior of the simulated result. In fact, the realized array gain with $\phi_s = 45°$ around 30 GHz is higher than that of $\phi_s = 45°$ which is not general for conventional antennas. It is because the active element pattern has a peak gain at off-broadside (actually, around ±45°) due to the strong mutual coupling by the adjacent elements.

TABLE II
PERFORMANCE COMPARISON OF ENDFIRE AND DUAL-POLARIZED MILLIMETER-WAVE LINEAR ARRAY ANTENNAS

Reference	Array	Fabrication	Array size[1] (λ_{low}^3)	Polarization	Bandwidth[2] (%)	Peak gain (dBi) (VP/HP)	Scanning range[3] (VP/HP)
[9]	1 × 4	PCB + Metal	3.2 × 3.0 × 0.9	VP	22.5 – 32 GHz (34.9)	14.8	35° (peak gain – 3 dB)
[10]	1 × 8	PCB + Metal	5.2 × 0.9 × (0.45 + α*)	VP	55.3 – 66.9 GHz (19.0)	9.0	56° (peak gain – 5 dB)
[11]	1 × 16	PCB + Metal	3.3 × 2.0 × 0.51	VP	15.4 – 46.4 GHz (100)	19.2	45° (VSWR < 4)
[13]	1 × 4	PCB	2.4 × 1.0 × 0.18	VP + HP	24.5 – 29.5 GHz (18.5)	10.3/11.3	50°/ 50° (peak gain – 4 dB)
[14]	1 × 4	PCB	2.8 × 0.7 × 0.13	VP + HP	25.0 – 29.5 GHz (16.5)	9.1/9.9	44°/ 44° (peak gain – 3 dB)
[15]	1 × 4	PCB	2.2 × 0.4 × 0.12	VP + HP	27.4 – 31.0 GHz (12.3)	8.0/9.2	NG
[16]	1 × 4	PCB	3.2 × 0.9 × 0.18	VP + HP	24.4 – 29.5 GHz (18.9)	9.16/9.27	33°/ 33° (peak gain – 3 dB)
[17]	1 × 8	PCB + Metal	5.9 × 1.2 × 0.55	VP + HP	24.8 – 32.5 GHz (26.9)	15.0/16.5	NG
This work	1 × 4	PCB + Metal	0.8 × 0.6 × 0.31	VP + HP	23.8 – 42.3 GHz (56)	8.0/8.2	45°/ 45° (TARC < -6 dB)

[1]Array direction × longitudinal direction × thickness at the lowest operating frequency.
[2]Overlapped bandwidth of both polarization and it is based on the broadside radiation.
[3]Scanning range is defined by the (criteria).
*: Not given metal thickness.
NG: Not given.

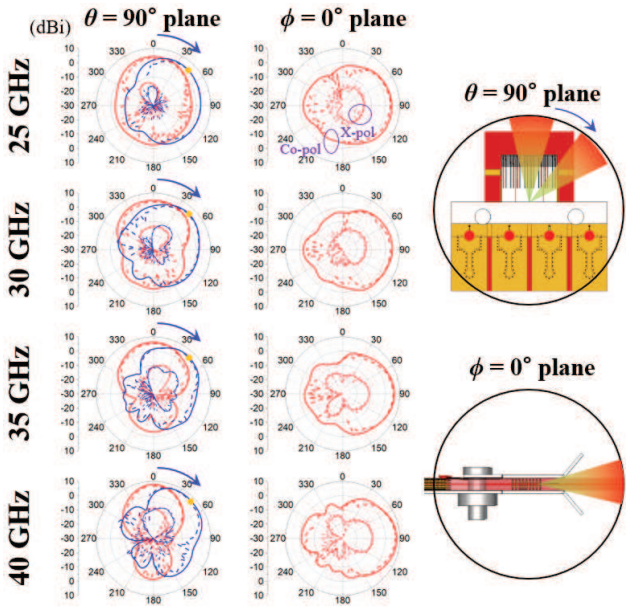

Fig. 13. Simulated (solid) and measured (dashed) V-pol gain patterns at various frequencies as scanning the beam from ϕ_s = 0° (red) to ϕ_s = 45° (blue). Strong and weak level patterns are corresponding to copolarization and cross-polarization, respectively.

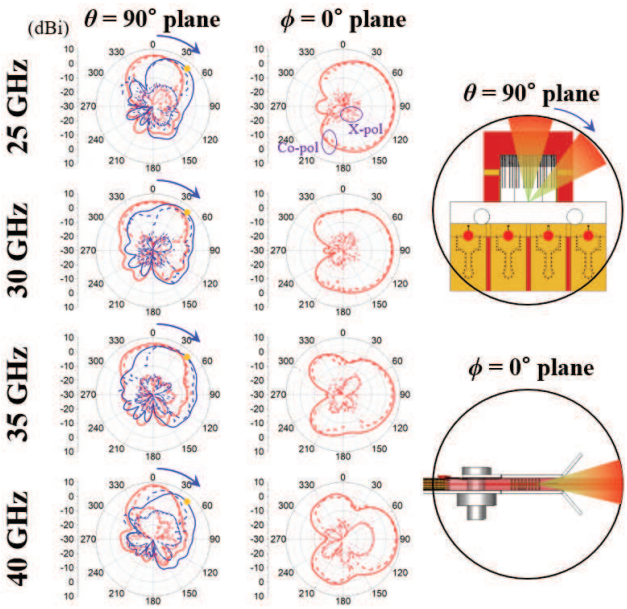

Fig. 14. Simulated (solid) and measured (dashed) H-pol gain patterns at various frequencies as scanning the beam from ϕ_s = 0° (red) to ϕ_s = 45° (blue). Strong and weak level patterns are corresponding to copolarization and cross-polarization, respectively.

Figs. 13 and 14 present simulated and measured radiation patterns for both the polarizations at several frequencies on two planes. In this context, θ = 90° plane represents the xy plane, where the gain is plotted against ϕ. And ϕ = 0° plane represents the xz plane, where the gain is plotted against θ. On the θ = 90° plane, when comparing both the polarizations, 3-dB beamwidth of the V-pol gain is wider than that of the H-pol gain. The reason is that on θ = 90° plane, a vertically polarized monopole has omnidirectional radiation pattern, and a horizontally polarized dipole has $\pm x$-directional radiation pattern. On the ϕ = 0° plane, 3-dB beamwidth of the H-pol gain is wider than that of the V-pol gain since the slotted horn renders the beam pattern to be more directive in the plane. Even with the presence of slotted horn, the main beams of both the polarizations can be steered up to ϕ_s = 45° on the θ = 90° plane. Although the feeding cables may cause some distortion in the radiation pattern and there are slight differences in the backside patterns, the measured results show

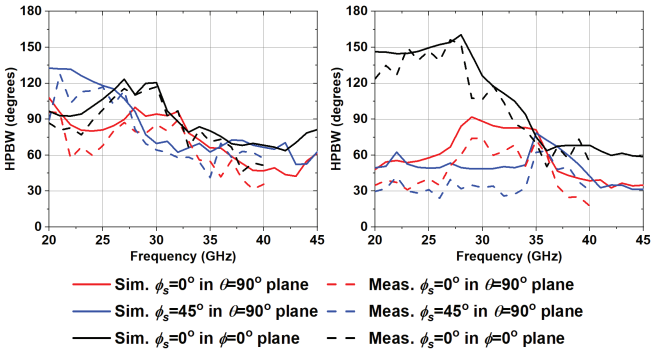

Fig. 15. Simulated (solid) and measured (dashed) HPBWs of the gain patterns at various frequencies as scanning the beam from $\phi_s = 0°$ (red) to $\phi_s = 45°$ (blue) in two planes. Left and right columns are corresponding to the TCMPA and the TCDA, respectively.

good agreement with the simulated ones. Fig. 15 presents half power beamwidth (HPBW) of the gain patterns at various frequencies as scanning the beam in two planes. The measured HPBW is in good agreement with the simulated result. Due to very thin configuration, the HPBW is very wide in $\phi = 0°$ plane. In general, the HPBW becomes wider as scanning the beam since the effective aperture becomes smaller. However, as mentioned before, the HPBW at $\phi_s = 45°$ in this case, which is directly related to the gain, is slightly narrower than that of $\phi_s = 0°$ at some frequencies due to active element patterns.

Performance of the proposed array is compared with the state-of-the-art endfire and dual-polarized mmWave linear array antennas in Table II. Here, three types of antennas are presented: vertically polarized antennas designed by metal objects and a PCB, dual-polarized antennas designed by only a PCB, and dual-polarized antennas designed by metal objects and a PCB. Wideband operation is challenging for antennas that operate primarily with vertical polarization. Therefore, metal objects are introduced to achieve wideband operation for vertically polarized antennas [9], [10], [11]. Especially for [11], it achieves a bandwidth of 100% and a peak gain of 19.2 dBi. However, it is by virtue of a thick and very long tapered metallic horn optimized for both bandwidth and gain. The second type of antennas [13], [14], [15], [16] has a thin configuration, but they exhibit a very narrow bandwidth less than 19% where the impedance bandwidth in this table is defined as the band satisfying reflection coefficient <–10 dB or VSWR < 2 for broadside radiation. In our work, as of the third type, the thickness of the proposed array is 0.31 λ_{low} which is significantly thinner compared with the first and third types of antennas. At the same time, the bandwidth is much wider than others, except for the work [11]. Furthermore, stable gains and scanning performance are demonstrated over a wide range.

IV. Conclusion

In this article, we proposed a wideband dual-polarized endfire array antenna that integrates a TCDA and a TCMPA within the same compact aperture for 5G mmWave applications. Unlike conventional dual-polarized structures that suffer from narrow bandwidth or bulky configurations, the proposed array achieves simultaneous and independent operation of vertical and horizontal polarizations over a wide frequency range using a set of polarization-selective structures—including a V-reflector, H-reflector, and a slotted horn radiator. Through detailed parametric studies and analysis of field distribution, we verified that the polarization-selective architecture allows for independent optimization of boundary conditions and reflector distances for each polarization. The proposed array successfully covers the 23.8–42.3-GHz band, which accounts for most of the FR 2 spectrum. The simulated and measured results confirm the excellent impedance matching and stable gain performance across the entire band. Compared with state-of-the-art designs, the proposed array offers superior bandwidth, thin profile, and improved polarization isolation within a shared aperture—making it a promising solution for high-capacity, robust wireless communication systems in the 5G FR 2 band and beyond.

References

[1] T. S. Rappaport et al., "Millimeter wave mobile communications for 5G cellular: It will work!," *IEEE Access*, vol. 1, pp. 335–349, 2013.

[2] G. Oliveri et al., "Codesign of unconventional array architectures and antenna elements for 5G base stations," *IEEE Trans. Antennas Propag.*, vol. 65, no. 12, pp. 6752–6767, Dec. 2017.

[3] J. Kornprobst, T. J. Mittermaier, and T. F. Eibert, "A millimeter-wave self-mixing array with large gain and wide angular receiving range," *IEEE Trans. Antennas Propag.*, vol. 66, no. 2, pp. 702–711, Feb. 2018.

[4] Y. Wang, H. Duan, L. He, X. Wu, D. Wang, and L. Li, "Design of 39-GHz up{-} and down-conversion mixers for 5G mmWave TDD applications," *J. Electromagn. Eng. Sci.*, vol. 23, no. 2, pp. 101–108, Mar. 2023.

[5] M.-S. Park, J. Cho, S. Lee, Y. Kwon, and K.-Y. Jung, "New measurement technique for complex permittivity in millimeter-wave band using simple rectangular waveguide adapters," *J. Electromagn. Eng. Sci.*, vol. 22, no. 6, pp. 616–621, Nov. 2022.

[6] *User Equipment (UE) Radio Transmission and Reception; Part 2: Range 2 Standalone (Release 15)*, document TS38.101-2 v15.0.0, Jun. 2018.

[7] R. J. Mailloux, *Phased Array Antenna Handbook*. Norwood, MA, USA: Artech House, 2017.

[8] W. El-Halwagy, R. Mirzavand, J. Melzer, M. Hossain, and P. Mousavi, "Investigation of wideband substrate-integrated vertically-polarized electric dipole antenna and arrays for mm-wave 5G mobile devices," *IEEE Access*, vol. 6, pp. 2145–2157, 2018.

[9] B. Yang, Z. Yu, Y. Dong, J. Zhou, and W. Hong, "Compact tapered slot antenna array for 5G millimeter-wave massive MIMO systems," *IEEE Trans. Antennas Propag.*, vol. 65, no. 12, pp. 6721–6727, Dec. 2017.

[10] Y. Li and K.-M. Luk, "A multibeam end-fire magnetoelectric dipole antenna array for millimeter-wave applications," *IEEE Trans. Antennas Propag.*, vol. 64, no. 7, pp. 2894–2904, Jul. 2016.

[11] A. Li and K.-M. Luk, "Ultra-wideband endfire long-slot-excited phased array for millimeter-wave applications," *IEEE Trans. Antennas Propag.*, vol. 69, no. 6, pp. 3284–3293, Jun. 2021.

[12] R. F. Harrington, "Effect of antenna size on gain, bandwidth, and efficiency," *J. Res. Nat. Bur. Standards, D, Radio Propag.*, vol. 64D, no. 1, pp. 1–12, Jan. 1960.

[13] L. Sun, Y. Li, and Z. Zhang, "Wideband dual-polarized endfire antenna based on compact open-ended cavity for 5G mm-wave mobile phones," *IEEE Trans. Antennas Propag.*, vol. 70, no. 3, pp. 1632–1642, Mar. 2022.

[14] M. Faizi Khajeim, G. Moradi, R. Sarraf Shirazi, and S. Zhang, "Broadband dual-polarized antenna array with endfire radiation for 5G mobile phone applications," *IEEE Antennas Wireless Propag. Lett.*, vol. 20, pp. 2427–2431, 2021.

[15] H.-T. Chou, S.-J. Chou, J. D. S. Deng, C.-H. Chang, and Z.-D. Yan, "LTCC-based antenna-in-package array for 5G user equipment with dual-polarized endfire radiations at millimeter-wave frequencies," *IEEE Trans. Antennas Propag.*, vol. 70, no. 4, pp. 3076–3081, Apr. 2022.

[16] H. Li, Y. Li, L. Chang, W. Sun, X. Qin, and H. Wang, "A wideband dual-polarized endfire antenna array with overlapped apertures and small clearance for 5G millimeter-wave applications," *IEEE Trans. Antennas Propag.*, vol. 69, no. 2, pp. 815–824, Feb. 2021.

[17] K. Sun et al., "Dual-polarized millimeter-wave endfire array based on substrate integrated mode-composite transmission line," *IEEE Trans. Antennas Propag.*, vol. 70, no. 1, pp. 341–352, Jan. 2022.
[18] H.-J. Dong, Y.-B. Kim, J. Joung, and H. L. Lee, "High gain and low-profile stacked magneto-electric dipole antenna for phased array beamforming," *IEEE Access*, vol. 8, pp. 180295–180304, 2020.
[19] J. L. Volakis and K. Sertel, "Narrowband and wideband metamaterial antennas based on degenerate band edge and magnetic photonic crystals," *Proc. IEEE*, vol. 99, no. 10, pp. 1732–1745, Oct. 2011.
[20] B. A. Munk, *Finite Antenna Arrays and FSS*. Hoboken, NJ, USA: Wiley, 2003.
[21] S. Kim and S. Nam, "Wideband vertically polarized endfire metasurface antenna fed by tightly coupled monopole probe array," *IEEE Trans. Antennas Propag.*, vol. 72, no. 3, pp. 2481–2489, Mar. 2024.
[22] S. S. Holland and M. N. Vouvakis, "The planar ultrawideband modular antenna (PUMA) array," *IEEE Trans. Antennas Propag.*, vol. 60, no. 1, pp. 130–140, Jan. 2012.
[23] C. A. Balanis, *Antenna Theory: Analysis and Design*. Hoboken, NJ, USA: Wiley, 2016.
[24] S. Kim and S. Nam, "Extremely low-profile wideband array antenna using TCDA with polarization convertor," *Microw. Opt. Technol. Lett.*, vol. 63, no. 3, pp. 959–964, Mar. 2021.
[25] J. P. Doane, K. Sertel, and J. L. Volakis, "A wideband, wide scanning tightly coupled dipole array with integrated balun (TCDA-IB)," *IEEE Trans. Antennas Propag.*, vol. 61, no. 9, pp. 4538–4548, Sep. 2013.
[26] S. Kim and S. Nam, "Wideband and ultrathin 2*times*2 dipole array antenna for 5G mmWave applications," *IEEE Antennas Wireless Propag. Lett.*, vol. 21, pp. 2517–2521, 2022.
[27] D. F. Kelley and W. L. Stutzman, "Array antenna pattern modeling methods that include mutual coupling effects," *IEEE Trans. Antennas Propag.*, vol. 41, no. 12, pp. 1625–1632, Dec. 1993.

Seongjung Kim (Member, IEEE) received the B.S. degree in electronic and electrical engineering from Hongik University, Seoul, South Korea, in 2017, and the M.S. and Ph.D. degrees in electrical engineering and computer science from Seoul National University, Seoul, in 2023.

Since 2023, he has been a Staff Engineer at the Department of System Large Scale Integration, Samsung Electronics, Hwaseong, Gyeonggi, South Korea. His main research interests are phased array antenna theory and design.

Young-Seok Lee (Graduate Student Member, IEEE) received the B.S. degree from the School of Electrical Engineering, Korea University, Seoul, South Korea, in 2021, and the M.S. degree from the Department of Electrical and Computer Engineering, Seoul National University, Seoul, in 2023, where he is currently pursuing the Ph.D. degree.

His current research interests include wireless power transfer systems, optimization algorithms, target detection, and indoor localization.

Sangwook Nam (Life Senior Member, IEEE) received the B.S. degree in electrical engineering from Seoul National University, Seoul, South Korea, in 1981, the M.S. degree in electrical engineering from Korea Advanced Institute of Science and Technology (KAIST), Daejeon, South Korea, in 1983, and the Ph.D. degree in electrical engineering from the University of Texas at Austin, Austin, TX, USA, in 1989.

From 1983 to 1986, he worked as a Researcher at the Gold Star Central Research Laboratory, Seoul. Since 1990, he has been a Professor with the School of Electrical Engineering and Computer Science, Seoul National University. His research interests include analysis/design of electromagnetic structures, antennas, and microwave active/passive circuits.